



## ARTICLE

# On-chip determination of tissue-specific metastatic potential of breast cancer cells

Burcu Firatligil-Yildirim<sup>1</sup> | Gizem Bati-Ayaz<sup>2</sup> | Ismail Tahmaz<sup>2</sup> | Muge Bilgen<sup>2</sup> |  
Devrim Pesen-Okvur<sup>1</sup>  | Ozden Yalcin-Ozuysal<sup>1</sup> 

<sup>1</sup>Department of Molecular Biology and Genetics, Izmir Institute of Technology, Izmir, Turkey

<sup>2</sup>Izmir Institute of Technology, Biotechnology and Bioengineering Graduate Program, Izmir, Turkey

## Correspondence

Devrim Pesen-Okvur and Ozden Yalcin-Ozuysal, Izmir Yüksek Teknoloji Enstitüsü, Moleküler Biyoloji ve Genetik Bölümü, 35430, Urla, Izmir, Turkey.

Email: [devrimpesen@iyte.edu.tr](mailto:devrimpesen@iyte.edu.tr) and [ozdenyalcin@iyte.edu.tr](mailto:ozdenyalcin@iyte.edu.tr)

## Funding information

Türkiye Bilimsel ve Teknolojik Arastırma Kurumu, Grant/Award Number: 115E057

## Abstract

Metastasis is one of the major obstacles for breast cancer patients. Limitations of current models demand the development of custom platforms to predict metastatic potential and homing choices of cancer cells. Here, two organ-on-chip platforms, invasion/chemotaxis (IC-chip) and extravasation (EX-chip) were used for the quantitative assessment of invasion and extravasation towards specific tissues. Lung, liver and breast microenvironments were simulated in the chips using tissue-specific cells embedded in matrigel. In the IC-chip, invasive MDA-MB-231, but not non-invasive MCF-7 breast cancer cells invaded into lung and liver microenvironments. In the EX-chip, MDA-MB-231 cells extravasated more into the lung compared to the liver and breast microenvironments. In addition, lung-specific MDA-MB-231 clone invaded and extravasated into the lung microenvironment more efficiently than the bone-specific clone. Both invasion/chemotaxis and extravasation results were in agreement with published clinical data. Collectively, our results show that IC-chip and EX-chip, simulating tissue-specific microenvironments, can distinguish different in vivo metastatic phenotypes, in vitro. Determination of tissue-specific metastatic potential of breast cancer cells is expected to improve diagnosis and help select the ideal therapy.

## KEYWORDS

breast cancer, extravasation, invasion, lab-on-a-chip, metastasis

## 1 | INTRODUCTION

Metastasis is the main cause of breast cancer mortality among women. The latest statistics revealed that the 5-year relative survival rate for women with metastatic breast cancer is around 26% between 1975 and 2017 (Howlander et al., 2020). Breast cancer frequently metastasizes to bone, lung, liver and brain. Although the molecular and histopathological subtypes of the tumor provide information on the metastasis risk and the target organs, there is no

diagnostic tool available that can accurately predict the risk and the organ preference for an individual patient's tumor. The target organ for metastasis is specified by both physiological architectures of the circulatory system and molecular determinants. It was first hypothesized by Stephan Paget in the 19th century that metastasizing tumor cells grow preferentially in specific target organs in a similar manner that a "seed" grows only in a suitable "soil" (Paget, 1889). Since then, experimental evidence has been supporting the "seed and soil" hypothesis by showing that molecular determinants on primary

Burcu Firatligil-Yildirim and Gizem Bati-Ayaz contributed equally to this study.

tumor and microenvironment of the target tissue are involved in the establishment of metastasis patterns (Langley & Fidler, 2011). Thus, a platform that integrates the information coming from tumor cells and the target organs would provide a diagnostic tool that can estimate the likeness of metastasis for a given tumor cell population towards specific environments.

The metastasis cascade is a complex phenomenon that includes in series, invasion, migration, intravasation and extravasation. The invasion process starts when cancer cells dissociate from their primary sites after losing cell-cell adhesion capacity and invade the surrounding stroma, while the extravasation process involves interactions between cancer cells and endothelial cells, where cancer cells pass through the endothelial layer into the target organ (Fares et al., 2020). Here, we focus on invasion and extravasation steps of the cascade to predict the metastatic potential of the cells towards different environments.

*In vivo* animal models have been used for the investigation of the metastatic process. However, they do not match the clinical progression, are costly, require months to reach results and are limited in throughput (Kimura et al., 2018). The Boyden chamber and transwell systems are the most favored *in vitro* platforms to study invasion and extravasation due to their simplicity. However, they use artificial barrier membranes that do not allow detailed visualization of cellular behavior at multiple time points. On the other hand, organ-on-chip (OoC) systems have low fabrication costs, can generate results within days, allow 3D cell culture of human cells, are compatible with various microscopy techniques and thus are well suited for spatial and temporal quantitative data analysis. OoC systems that can mimic the *in vivo* microenvironment present great advantages for *in vitro* strategies and therefore they have a huge potential to minimize animal testing in the preclinical research area (Rodrigues et al., 2020; Soscia et al., 2017; Wu et al., 2020).

*In vitro* OoC models were developed to investigate different factors involved in metastasis such as intravasation (Shirure et al., 2018; Song et al., 2009; Truong et al., 2016), angiogenesis (Bi et al., 2020; Shirure et al., 2018; Vickerman & Kamm, 2012) the interaction between tumor cells and endothelial cells with stromal cells and immune cells (Bi et al., 2020; Boussoimmier-Calleja et al., 2019; Zervantonakis et al., 2012), the interstitial flow (Polacheck et al., 2011), matrix stiffness (Pathak & Kumar, 2012), and extravasation (Bersini et al., 2014; Boussoimmier-Calleja et al., 2019; Chen, Whisler, et al. (2017); Jeon et al., 2015). Target tissues such as bone (Bersini et al., 2014) and lung (Bi et al., 2020; Boussoimmier-Calleja et al., 2019; Shirure et al., 2018) were modelled in some of OoC models. However, assessment of tissue-specific invasion and extravasation in the context of the homing choices of cancer cells has been lacking. Here, two OoC platforms, invasion/chemotaxis (IC-chip) and extravasation (EX-chip) were used for the quantitative and comparative assessment of invasion and extravasation into microenvironments simulating specific tissues relevant to the breast cancer metastasis.

## 2 | MATERIALS AND METHODS

### 2.1 | Lab-on-a-chip fabrication

Invasion-chemotaxis and extravasation lab-on-a-chip platforms (IC-chip and EX-chip) (Figure S1, Supporting Information) were either provided by Initio Biomedical Engineering (Turkey) or fabricated by soft lithography as previously described (Ozdil et al., 2014). Briefly, SU-8 polymer was spin-coated on a silicon wafer. The design of the chip was exposed through a mask to UV light. After removing the uncrosslinked SU8 polymer using the developer solution, molds were ready for polydimethylsiloxane (PDMS) casting. After PDMS polymerization, inlet and outlet holes were punched with biopsy punches. The PDMS parts were cleaned and bonded to clean microscope slides after treatment in UV/Ozone cleaner (Bioforce Nanosciences). The chips were sterilized with UV light in a laminar hood for 15 min before use. The dimensions of IC-chip: the homing matrix channel (HMC) 3 mm width × 12 mm length × 200 μm height and medium channels (MC1/MC2) 3 mm width × 12 mm length × 200 μm height; EX-chip: the HMC 3 mm width × 15 mm length × 200 μm height, endothelial monolayer channel (EMC) 3 mm width × 20 mm length × 200 μm height and medium channel (MC) 3 mm width × 10 mm length × 200 μm height.

### 2.2 | Chip surface modification

IC-chips were used without any surface modifications. EX-chips were first coated with either poly-L-lysine (PLL, P8920; Sigma-Aldrich) or 3-aminopropyltriethoxysilane (APTES, A3648; Sigma-Aldrich). EX-chips were incubated with PLL (0.01 mg ml<sup>-1</sup>) in ultra-pure water at 37°C in a 5% CO<sub>2</sub> incubator overnight. The following day, EX-chips were washed with ultra-pure water three times and then kept at 80°C for 24 h to reduce hydrophobicity of the surface. For APTES modification of surfaces, APTES (2%) dissolved in acetone was loaded into the channels of EX-chips and incubated for 15 min in laminar flow cabin. Then EX-chips were washed with first PBS once and then ultra-pure autoclaved H<sub>2</sub>O three times. At this step, EX-chips were ready to be coated with extracellular matrix proteins: laminin (LAM), type I collagen (COL) or FN. LAM (0.0125 mg ml<sup>-1</sup>, L2020; Sigma-Aldrich) and FN (0.0125 mg ml<sup>-1</sup>, F2006, Sigma-Aldrich) were prepared in 1X Universal Buffer (UB), while COL (0.0125 mg ml<sup>-1</sup>, 354249; Corning) was diluted in serum-free DMEM (Biological Industries; 01-055-1A). Each protein solution was loaded into EX-chips and they were incubated at 37°C in a 5% CO<sub>2</sub> incubator for 1 h. LAM- and FN-coated EX-chips were washed first with PBS once and then with ultra-pure autoclaved H<sub>2</sub>O three times. COL-coated EX-chips were washed first with serum-free DMEM and then ultra-pure autoclaved H<sub>2</sub>O for three times. Any remaining H<sub>2</sub>O was aspirated by vacuum. EX-chips were stored in vacuum desiccators at least one day before use in experiments. APTES-LAM-coated EX-chips were used in all extravasation assays (Figure S1b, Supporting Information).

### 2.3 | Cell lines

Human breast cancer cell lines (MDA-MB-231 and MCF-7), human normal mammary epithelial cell line (MCF-10A), human normal lung fibroblast cell line (WI-38), rat normal liver cell line (BRL-3A), and human umbilical vein endothelial cell line (HUVEC-C) were obtained from ATCC. Organ-specific metastatic clones of MDA-MB-231, MDA-MB-231 LM2 and MDA-MB-231 1833-BoM were described previously (Bos et al., 2009; Kang et al., 2005; Minn et al., 2005) and were gifts from the Joan Massagué Lab in Memorial Sloan Kettering Cancer Center. MDA-MB-231, its derivatives and MCF-7 were cultured in DMEM high glucose (11965092; Gibco) with fetal bovine serum (FBS, 10%) (A3840001; Gibco) and penicillin/streptomycin (15070063; Gibco; 1%); MCF-10A was cultured in DMEM-F12 high glucose (11330057; Gibco) with Horse Serum (04-004-1A; Biological Industries; 5%), Insulin (I9278; Sigma; 10  $\mu\text{g ml}^{-1}$ ), Cholera Toxin (C8052; Sigma; 100  $\text{ng ml}^{-1}$ ), EGF (E9644; Sigma; 20  $\text{ng ml}^{-1}$ ), Hydrocortisone (H0888; Sigma; 0.5  $\mu\text{g ml}^{-1}$ ) and penicillin/streptomycin (1%). WI-38 and BRL-3A were cultured in high glucose MEM- $\alpha$  (01-042-1A; Biological Industries) with FBS (10%) and penicillin/streptomycin (1%). HUVEC-C cell line was cultured in DMEM-F12K high glucose (01-095-1A, Biological Industries) with FBS (10%), heparin (H3393; Sigma; 0.1  $\text{mg ml}^{-1}$ ), endothelial cell growth supplement (EGCS, 0.05  $\text{mg ml}^{-1}$ ) (354006; Sigma) and penicillin/streptomycin (1%). All cell lines were cultured at 37°C in a humidified incubator with 5%  $\text{CO}_2$ .

### 2.4 | Labelling of cell lines

MDA-MB-231, metastatic clones of MDA-MB-231 (LM2 and 1833-BoM) and MCF-7 cancer cell lines were stably labelled with a red fluorescent protein (DsRed). MSCV retroviruses expressing both DsRed and puromycin resistance genes were used for infection. The preparation of viruses and infection of cells were performed as described previously (Yalcin-Ozuyal et al., 2010; Zengin et al., 2015). 48 h after infection, the antibiotic selection was carried out with puromycin (2  $\mu\text{g ml}^{-1}$ ) until all of the uninfected cells died. Transient labelling of HUVEC-C cells was performed by Green Cell Tracker CMFDA (C2925; Invitrogen). The dye was dissolved in dimethyl sulfoxide to obtain stock solution (25 mM) which was then diluted with serum-free DMEM-F12K media to get working concentration (5  $\mu\text{M}$ ). Cells were washed with warm PBS once, and then tracker (5  $\mu\text{M}$ ) was added over the cells. After 30 min of incubation at 37°C, the media was removed, cells were washed with PBS once and then complete HUVEC-C growth media was added. Labelling was performed 30 min before the experimental set-up.

### 2.5 | Invasion assay

IC-chips were used for invasion assays (Figure S1a). For cell-free assays, growth factor reduced matrigel (GFR-matrigel, 8  $\text{mg ml}^{-1}$ ) (354230; Corning) was diluted in 1:1 ratio with pre-cooled serum-

free media and loaded into the HMC of the chips. Then, chips were incubated for polymerization at 37°C in a humidified incubator with 5%  $\text{CO}_2$  for 30 min. After polymerization of GFR-matrigel, either serum-free or serum-containing media was loaded into the media channels 1 and 2 (MC1, MC2) and chips were incubated overnight. The following day, media in MC1 and MC2 were removed, channels were washed with serum-free media twice. Then serum-free (0%) or serum-containing media (10%) was added to MC2 of the chip for the relevant conditions. DsRed labelled MDA-MB-231 cells ( $1 \times 10^6$  cells  $\text{ml}^{-1}$ ) resuspended in serum-free media were added to MC1. The chips were incubated vertically for 3 days.

To analyze the effects of serum on invasion towards liver microenvironment, BRL-3A normal liver cells ( $1 \times 10^7$  cells  $\text{ml}^{-1}$ ) with GFR-matrigel were loaded to HMC of the IC-chips as explained above. Then, chips were incubated overnight with culture media with (2% or 10%) or without (0%) serum at both MC1 and MC2 channels. The following day, MC2 was loaded with serum-free media after washing the channel with serum-free media twice. DsRed labelled MDA-MB-231 cells ( $1 \times 10^6$  cells  $\text{ml}^{-1}$ ) in serum-free media, were added to the MC1 and incubated vertically for 3 days.

To analyze invasion towards specific tissues, lung, liver and breast microenvironments were modelled by tissue-specific normal cell lines WI-38, BRL-3A and MCF-10A, respectively. Two different cell densities ( $2.5 \times 10^6$  and  $5 \times 10^6$  cells  $\text{ml}^{-1}$  for WI38;  $1 \times 10^7$  and  $2 \times 10^7$  cells  $\text{ml}^{-1}$  for BRL3A) were tested for gene expression of factors involved in chemoattraction (CCL5, CXCL12, and IGF1) (Supporting Information). The cell density that provided higher cytokine expression levels was used for modeling the specific homing tissues. (Figure S2a and S2b, Supporting Information). MCF10A cells did not express any of the cytokines and they were seeded at a similar density to WI-38 cells. The cells seeded at the determined cell density organized into 3D structures in GFR-matrigel (Figure S2c, Supporting Information). Each cell line (BRL-3A:  $1 \times 10^7$  cells  $\text{ml}^{-1}$ , WI-38:  $5 \times 10^6$  cells  $\text{ml}^{-1}$ , MCF-10A:  $4.4 \times 10^6$  cells  $\text{ml}^{-1}$ ) was mixed with GFR-matrigel and loaded into the HMC of the IC-chips. The chips were incubated overnight with serum-free media in MC1 and MC2. The following day, media in MC2 was changed with fresh serum-free media. MDA-MB-231 or MCF-7 cells ( $1 \times 10^6$  cells  $\text{ml}^{-1}$ ) were seeded to MC1 in serum-free media. Chips were incubated vertically for 3 days. The invasion was visualized every 24 h by 3D imaging using a Leica SP8 confocal microscope.

### 2.6 | Analysis of invasion

Z-stack images of post-gaps of IC-chips were acquired each day with a  $\times 10$  objective and a z-step size of 7.52  $\mu\text{m}$ . The analysis of the acquired images was performed by Python programming and R Studio as previously explained (Ilhan et al., 2020). Briefly, the sum projection of z-stacks was thresholded and the distance of each bright pixel to the starting line of the invasion was calculated. The invasion capacity of the cells was determined through normalization of data sets to Day 1.

## 2.7 | Endothelial monolayer formation

HUVEC-C cells labelled with Green Cell Tracker CMFDA were collected from culture dishes following Trypsin EDTA Solution A (0.25%, 03-050-1B; Biological Industries) treatment for 5 min. After centrifugation, they were resuspended in 450–650 kDa dextran (8%, 31392; Sigma-Aldrich) in HUVEC-C media. The HUVEC-C cells ( $3.85 \times 10^6 \text{ ml}^{-1}$ ) were loaded to EMC of APTES-LAM-coated EX-chips. EX-chips were incubated vertically at 37°C in a humidified incubator with 5% CO<sub>2</sub> overnight. Endothelial monolayer formation was confirmed by 3D imaging using a Leica SP8 confocal microscope with a  $\times 10$  objective and a z-step size of 7.52  $\mu\text{m}$ .

## 2.8 | Actin staining for endothelial monolayer

Actin staining was performed to confirm the physical integrity of the endothelial cell monolayer. Cell-free GFR-matrigel (1:1 GFR-matrigel in serum-free media) was loaded to the HMC of the EX-chips. Following polymerization of matrigel, HUVEC-C cells were seeded to the EMC, culture media was loaded into the MC and chips were incubated overnight at 37°C in a humidified incubator with 5% CO<sub>2</sub>. The following day, media within EMC and MC was removed and paraformaldehyde (4%) was added to fix the sample. Then, the chip was incubated overnight at +4°C. The following day, the EMC and MC were washed with PBS ( $\times 1$ ) three times. Permeabilization solution (5% BSA and 0.1% Triton-X-100 in PBS buffer) was loaded to the EMC and MC and incubated at room temperature (RT) for 15 min. Then, the EMC and MC were washed with PBS ( $\times 1$ ) three times. Phalloidin (1:40, Alexa Fluor™ 647) (A22287; Invitrogen) for actin-filament staining and 4',6-diamidino-2-phenylindole (DAPI; 1:500) for nuclei staining diluted in PBS were loaded to the EMC and MC and the chip was incubated for one hour at RT in the dark. Finally, the EMC and MC were washed with PBS and then filled with anti-fading mounting media (90% glycerol, 10% PBS  $\times 10$ , 0.1 M or 2% (w/v) n-propyl gallate). The chip was kept at +4°C. The next day, images were acquired by a Leica SP8 confocal microscope (Figure 4c).

## 2.9 | Endothelial monolayer permeability assay

Fluorescently labelled 70-kDa dextran TR (D1830, Texas Red, neutral, Thermo Fisher Scientific) (final concentration 0.1 mg ml<sup>-1</sup>) was used for the measurement of endothelial monolayer permeability as described previously (van Duinen et al., 2017). 70-kDa dextran TR in PBS was loaded into the EMC. The chip was imaged using a Leica SP8 confocal microscope with  $\times 10$  objective. Images were captured every 10 min for up to 2 h. Images were then processed with ImageJ/Fiji and numerical analysis was performed using Excel. Fluorescence signal intensities were measured for the regions of interest drawn in the EMC and the HMC along the post gaps. Permeability ( $P$ ) was calculated according to  $P = [d(I_{\text{HMC}}/I_{\text{EMC}})/dt] * V_{\text{gel}} * 1/A$  where  $I_{\text{HMC}}$  and  $I_{\text{EMC}}$  are the fluorescence intensities in the HMC and EMC,

respectively;  $V_{\text{gel}}$  is the volume of the gel (10 mm<sup>3</sup>),  $A$  is the surface area of the post gap (0.06 mm<sup>2</sup>).

## 2.10 | Extravasation assay

EX-chips were used for extravasation assays (Figure S1b). The same protocols for environment generation in the invasion assay and endothelial monolayer formation were followed as explained above. Once the monolayer was formed by HUVEC-C cells, DsRed labelled MDA-MB-231 cells ( $1 \times 10^6 \text{ cells ml}^{-1}$ ) were seeded to the EMC in serum-free media for each condition (lung, liver and breast micro-environments) and the chips were incubated vertically for 3 days. The integrity of endothelial monolayer was confirmed by confocal microscopy immediately after addition of MDA-MB-231 cells. The extravasation of MDA-MB-231 cells to the generated lung, liver and breast microenvironments was visualized by 3D imaging using a Leica SP8 confocal microscope at  $\times 10$  magnification and a z-step size of 7.52  $\mu\text{m}$  for 3 days.

## 2.11 | Analysis of extravasation

Z-stack images of post gaps of EX-chips were acquired each day with a 10X objective and a z-step size of 7.52  $\mu\text{m}$ . The integrity of endothelial layer covering the post-gaps was confirmed by green signal for each time point. Cancer cells were marked as “extravasated” if they passed through the endothelial monolayer, or “associated” if they kept in contact with the endothelial monolayer. The efficiency of the EX-chips was quantified by the extravasation metric (EM), defined as the ratio of the number of post gaps with one or more extravasated cells to the total number of post gaps. If extravasation is observed in all ROIs, the EM will be 1. The  $\chi^2$  (Chi-squared) test was used for the statistical analysis of the EM.

## 2.12 | Statistical analysis

For each quantification, at least 3 post-gaps were analyzed. The number of post-gaps were indicated as “ $n$ ” in the figure legends. Results are reported mean  $\pm$  SEM unless otherwise noted. Student's  $t$  test was used for statistical analysis unless otherwise noted. A  $p$ -value of  $<.05$  was considered significant.

# 3 | RESULTS

## 3.1 | Effect of serum on the invasion/chemotaxis of breast cancer cells in the presence and absence of homing cells

Invasion/chemotaxis and extravasation are two crucial steps in cancer metastasis. The factors secreted from stromal cells

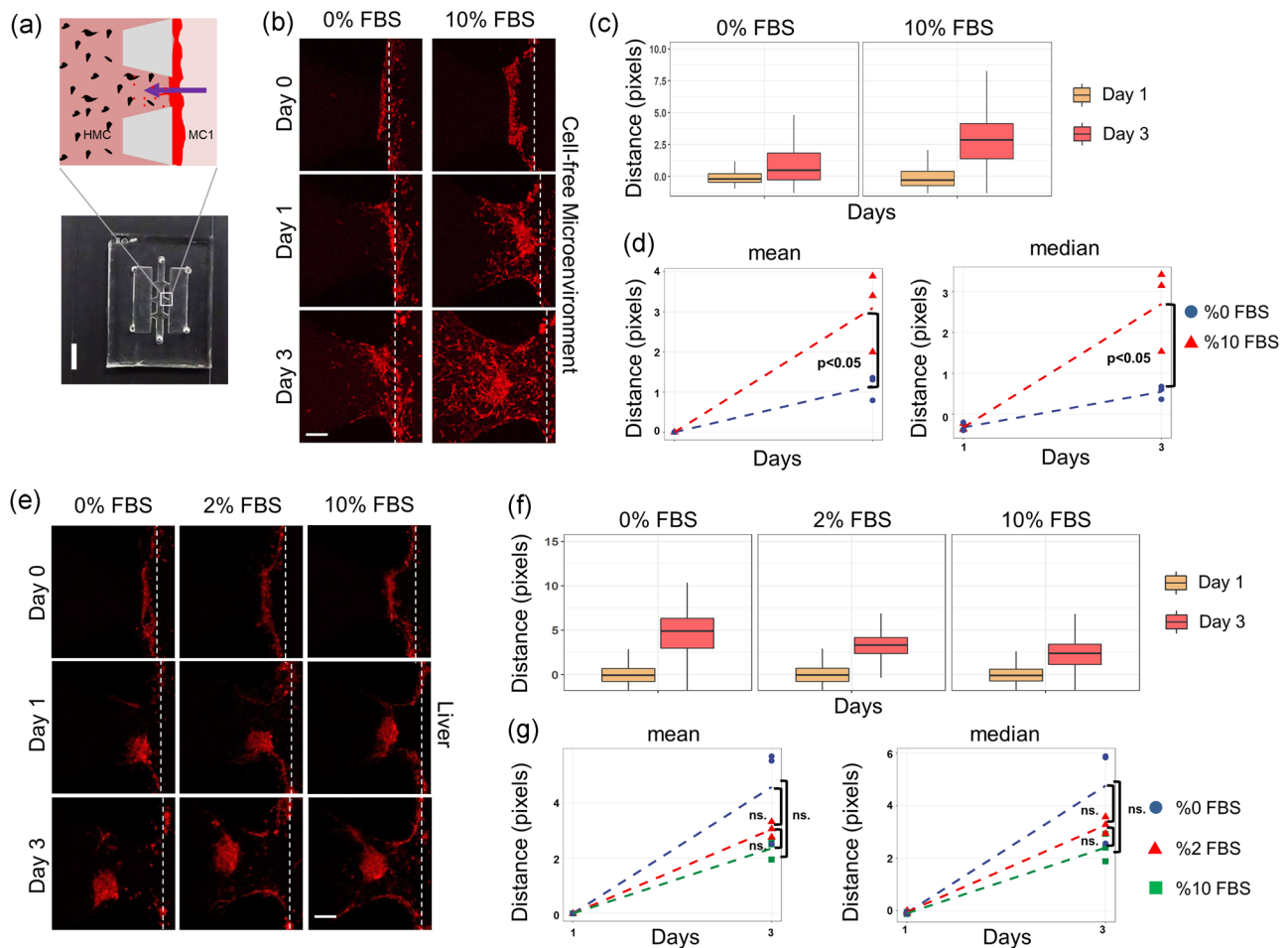


**FIGURE 1** Effect of serum on the invasion/chemotaxis of breast cancer cells in the presence and absence of homing cells. (a) Schematic representation of the invasion data, where homing channel (HMC) is loaded with growth factor reduced (GFR)-matrigel including homing cells or not and medium channel (MC1) is loaded with MDA-MB-231 cells; scale bar = 5 mm. Representative Z-stack projection images showing invasion/chemotaxis of MDA-MB-231 cells (red) towards (b) cell-free GFR-matrigel in the absence or presence fetal bovine serum (FBS), and (e) liver cell-laden GFR-matrigel in the presence of 0%, 2%, and 10% FBS; scale bar = 200  $\mu\text{m}$ . (c and f) Distribution of migration distances normalized to Day 1. (d and g) Mean and median values of normalized distance distributions. Data were normalized to Day 1 ( $n = 3$ ). The dashed lines in (b) and (e) correspond to the starting line of invasion/chemotaxis

residing within target tissue microenvironments play important roles in directing tumor cells towards specific target sites (Fares et al., 2020; Guo & Deng, 2018; Roussos et al., 2011). To investigate tissue-specific invasion/chemotaxis and extravasation, two different OoC devices were used (Figure S1, Supporting Information). The invasion/chemotaxis chip (IC-chip) comprised three channels: MC1, HMC, and MC2. The IC-chip was symmetric along the long axis of HMC so that a gradient of factors in the MC2 can be realized across the HMC from MC2 to MC1. The procedure for the invasion assay on the IC-chip is shown in Figure S1a. Here, cells loaded into the MC1 were expected to show invasion and chemotaxis in response to the microenvironment in the HMC and/or the contents of the MC2.

The extravasation-chip (EX-chip) also comprised three channels: endothelial monolayer channel (EMC), HMC, MC. However, the EMC and the MC were not mirror images of each other as was the case for

the MC1 and MC2 of the IC-chip. The EMC was a narrow channel designed to hold endothelial cells and intended to mimic a blood vessel. The procedure for the extravasation assay using the EX-chip is shown in Figure S1b. Here, cells loaded into the EMC after the formation of an intact endothelial monolayer were expected to show extravasation through the endothelial cells in response to the microenvironment in the HMC. In both the IC-chip and the EX-chip, the HMC was used to mimic the microenvironments of lung, liver or breast tissue, making it possible to assess tissue-specific invasion/chemotaxis and extravasation.

First, IC-chips with cell-free growth factor reduced (GFR)-matrigel in the HMC were used to examine invasion/chemotaxis of MDA-MB-231 cells using confocal fluorescence microscopy for 3 days (Figure 1a,b). Quantitative analysis of fluorescence images showed that invasion/chemotaxis increased from Day 1 to Day 3 for both 10% FBS (fetal bovine serum) and FBS-free conditions,

consistent with the invasive phenotype of triple-negative MDA-MB-231 cells (Figure 1c). However, MDA-MB-231 cells showed 2.7 fold more invasion/chemotaxis towards FBS (10%) containing media than towards FBS free medium ( $p < .05$ ), as expected (Figure 1d). A significant increase was detected in both the mean and the median distances invaded by the cells in 10% FBS condition compared to the FBS-free condition (Figure 1d). These results showed that the IC-chip can be used to quantitatively assay the invasion/chemotaxis phenotype of cells.

To optimize the invasion/chemotaxis assay towards different tissue microenvironments, the effect of serum in the presence of homing cells was tested. BRL-3A liver cells were resuspended in serum-free media, mixed with GFR-matrigel and loaded into the HMC. Medium (0%, 2% or 10% FBS) was added into the MC2. Invasion of MDA-MB-231 cells loaded into the MC1 towards the HMC was examined (Figure 1e). Quantitative image analysis showed that for all the three different FBS concentrations in the MC2, the invasion of MDA-MB-231 cells increased from Day 1 to Day 3 (Figure 1f). In addition, there were no significant differences in the invasion of MDA-MB-231 cells with 0%, 2% or 10% FBS containing medium in the MC2 when liver cells were present in the HMC (Figure 1g).

Therefore, the presence of homing cells such as BRL-3A was sufficient to induce invasion/chemotaxis of MDA-MB-231 cells. Consequently, serum-free media was used in the MC2 for all invasion experiments with cell-laden GFR-matrigel in the HMC. Altogether these results demonstrated that the IC-chip provided a robust platform for invasion/chemotaxis assays in the presence or absence of target tissue cells.

### 3.2 | Invasion/chemotaxis of breast cancer cells into the lung, liver and breast microenvironments

To distinguish invasion/chemotaxis to different tissues, WI-38, BRL-3A and MCF-10A cell-laden GFR-matrigel was used in the HMC of the IC-chips to simulate the lung, liver and breast microenvironments, respectively. The distance MDA-MB-231 cells invaded towards all the three (lung, liver and breast) microenvironments increased from Day 1 to Day 3 as expected due to the known metastatic phenotype of these cells (Figures 2a,b). However, the invasion of MDA-MB-231 cells to the lung and liver microenvironments was significantly 2.4 and 2.1 fold higher than that to the breast microenvironment, respectively (Figure 2c and Table S1, Supporting Information). MCF-7 cells did not significantly invade towards lung, liver or breast environments up to Day 3, as expected due to the known non-metastatic phenotype of these cells, having no preference for different homing tissues (Figures 2d-f). These data showing that MDA-MB-231 cells had a higher preference of invasion to the lung and liver microenvironments than the breast microenvironment are in agreement with published clinical data for homing choices of breast cancer (M.-T. Chen, Sun, et al., 2017; Wang et al., 2019).

### 3.3 | Invasion/chemotaxis of lung-specific and bone-specific metastatic breast cancer cells into the lung microenvironment

Lungs are the most common sites of breast cancer metastasis (Jin et al., 2018). Therefore, we examined the invasion/chemotaxis of organ-specific metastatic clones of MDA-MB-231 cells for lung (MDA-MB-231 LM2) and bone (MDA-MB-231 1833-BoM) (Bos et al., 2009; Kang et al., 2005; Minn et al., 2005) towards the lung microenvironment in the IC-chip. Parental and lung-specific (LM2) MDA-MB-231 cells invaded the lung microenvironment remarkably well, while bone-specific (BoM 1833) cells moved marginally towards HMC (Figure 3a,b). The distance invaded by parental and lung-specific cells were 16- and 12-fold higher than that by the bone-specific cells, respectively (Figure 3c and Table S1, Supporting Information). Taken together, these data showed that the IC-chip simulating different tissue microenvironments can successfully and quantitatively demonstrate invasion/chemotaxis and homing choices of breast cancer cells with different *in vivo* metastatic site preferences.

### 3.4 | Generation of an intact endothelial monolayer

The interior surfaces of EX-chips were chemically and biochemically modified to ensure the attachment of endothelial cells for the generation of an intact monolayer. Here, 3-aminopropyl triethoxysilane (APTES) and poly-L-lysine solution (PLL) were tested for their ability to promote FN coating. Both APTES and PLL supported FN coating and thus efficient endothelial cell monolayer formation. (Figure S3b, Supporting Information). APTES coating was preferred due to the shorter application time. To enhance formation of an intact endothelial monolayer, laminin (LAM), collagen type I (COL), and FN were tested on APTES pre-coated interior PDMS surfaces of EX-chips. LAM-coated surfaces provided the most appropriate surfaces for the attachment of endothelial cells that covered a larger area (Figures 4a,b). In addition, when endothelial cells were loaded into EMC, they tend to form clusters. Thus, dextran was used in the cell resuspension medium to inhibit cluster formation and ensure a homogeneous distribution of endothelial cells in the EMC (Figure S3a, Supporting Information) (Myers et al., 2012). Intact endothelial monolayer formation was confirmed by staining the cytoskeleton of endothelial cells, specifically, actin filaments (Figure 4c). Fluorescence signal coming from Green Cell Tracker labelled HUVEC-C cells was sparse. However, actin staining confirmed the confluence of the endothelial monolayer. These results suggested that the green signal obtained by transient labelling of cells by the Green Cell Tracker might not reflect the extent of HUVEC-C coverage on the surface. Intact endothelial monolayer formation was further demonstrated by measuring diffusion of fluorescent 70-kDa dextran from the EMC to the

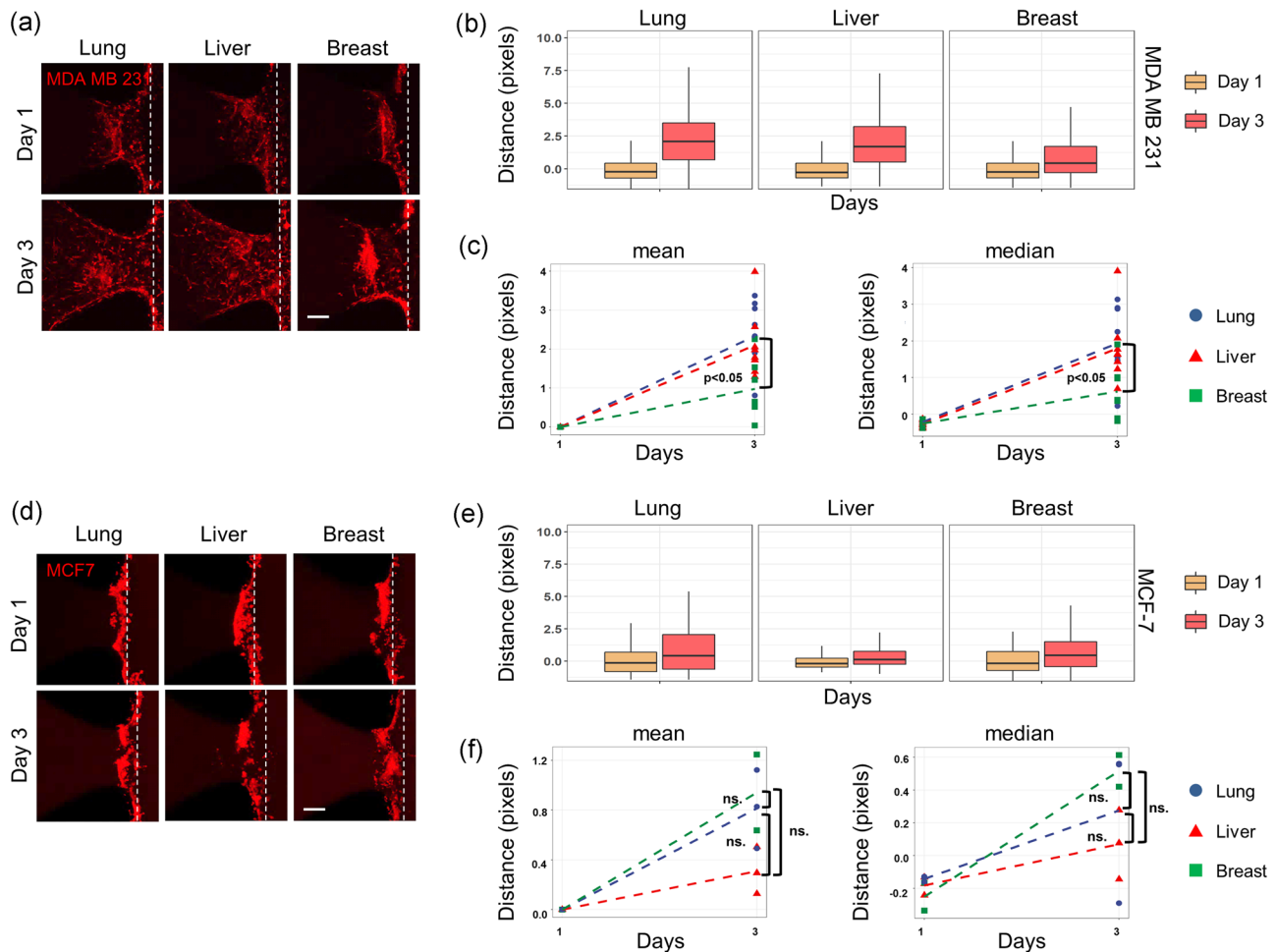


**FIGURE 2** Invasion/chemotaxis of breast cancer cells into the lung, liver and breast microenvironments. Representative Z-stack projection images showing invasion/chemotaxis of (a) MDA-MB-231 cells (red) and (d) MCF7 cells (red) to the lung, liver and breast microenvironments. (b and e) Distribution of migration distances normalized to Day 1. (c and f) Mean and median values of normalized distance distributions. Data were normalized to Day 1;  $n = 6$ . The dashed lines in (a) and (b) correspond to the starting line of invasion/chemotaxis. Scale bar = 200  $\mu\text{m}$

HMC in the presence and absence of endothelial cells (Figure 4d,e). Permeability calculations showed that presence of an endothelial monolayer significantly reduced diffusion of fluorescent 70 kDa dextran from  $3.12 \pm 0.63 \times 10^{-5}$  to  $0.88 \pm 0.1 \times 10^{-5} \text{ cm s}^{-1}$  (Figure 4f), in agreement with the previous studies (Frost et al., 2019; Jeon et al., 2013; van Duinen et al., 2017; Zervantonakis et al., 2012). Taken together, these results demonstrated that an intact endothelial monolayer with low permeability can be realized in EX-chips.

### 3.5 | Extravasation of metastatic breast cancer cells into the lung, liver and breast microenvironments

To distinguish extravasation and homing choices of breast cancer cells, the lung, liver and breast microenvironments were generated in the HMC, while an intact endothelial monolayer was realized in the EMC of the EX-chip. Extravasation was comparatively and

quantitatively determined (Figures 5a,b,d). The efficiency of the EX-chips was quantified by the EM. The EM for the lung, liver and breast microenvironments were 0.89, 1 and 0.89, respectively, with no statistically significant differences between different microenvironments, showing that extravasation events were observed in almost all post gaps independent from the homing microenvironment. Cancer cells that passed through the endothelial layer were considered as extravasated, while cells that were detected within the endothelial layer were considered as associated. The number of extravasated cells were the highest in the lung, less in the liver and the lowest in the breast microenvironments. (Figure 5d and Table S1, Supporting Information). Numbers of MDA-MB-231 cells that remained associated with the endothelial monolayer were highest when the HMC contained the breast microenvironment (Figure 5d and Table S1, Supporting Information). Furthermore, the number of extravasated lung-specific MDA-MB-231 cells (LM2) were significantly higher than that of bone-specific (BoM 1833) cells towards lung microenvironment, while associated cell numbers were similar (Figure 5c,e and Table S1, Supporting Information). Taken together,

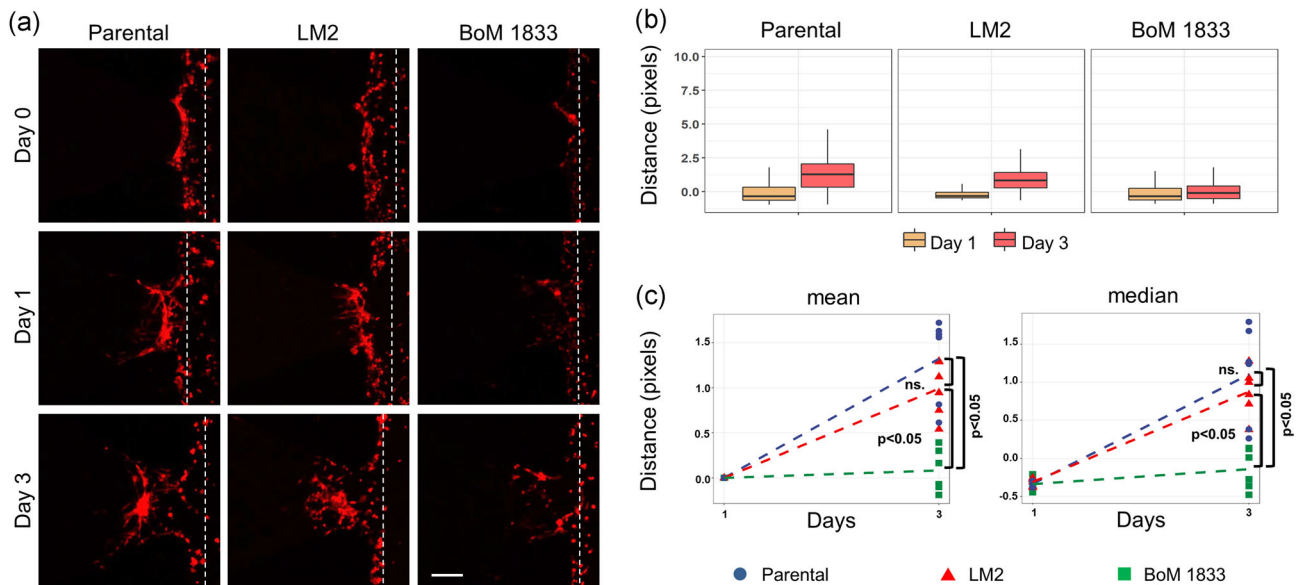


**FIGURE 3** Invasion/chemotaxis of lung- and bone-specific metastatic breast cancer cells into the lung microenvironment. (a) Representative Z-stack projection images showing invasion/chemotaxis of parental, LM2 (lung-specific) and BoM 1833 (bone-specific) MDA-MB-231 cells (red) to the lung microenvironment generated by WI-38 cell line (dashed line corresponds to the starting line for invasion; scale bar = 200  $\mu\text{m}$ ). (b) The distance of each bright pixel to the starting line (dashed) was calculated after thresholding of Z-stack images. The data normalized to day 1 were plotted ( $n = 3$ ). (c) Mean and median values of normalized distance distributions were plotted for Days 1 and 3 ( $n = 3$ )

these results showed that the EX-chip can demonstrate and quantify homing choices of the extravasating breast cancer cells.

## 4 | DISCUSSION

Microfluidic platforms such as OoC systems are promising tools expected to reduce and complement not only animal studies but also clinical trials (Peck et al., 2020; van Den Berg et al., 2019). Therefore, it is vital to develop OoC systems that can comparatively and quantitatively assess metastatic potential and homing choices of cancer cells. Here, we introduced two novel OoC systems that enable the visualization and quantification of tissue-specific breast cancer invasion/chemotaxis and extravasation. We generated lung, liver and breast microenvironments that simulate the well-known homing tissues for metastatic breast cancer cells and quantitatively distinguished the invasion/chemotaxis and extravasation phenotypes of different breast cancer cell lines.

Several OoC platforms using normal human lung fibroblasts were developed to model lung microenvironment and assessed intravasation, extravasation, angiogenesis, drug response and proliferation of cancer cells (Bi et al., 2020; Boussommier-Calleja et al., 2019; Shirure et al., 2018). These microenvironments included microvascular networks formed by HUVEC or cord blood-derived endothelial cells, which allowed trapping of cancer cells and physiological delivery of nutrients or drugs. Similar to a previous study that modeled bone microenvironment to assess extravasation (Bersini et al., 2014), we generated an endothelial monolayer separating cancer cells from the

homing cells, where physical limitations of the capillary network are not present. The OoC platforms we used in this study reduced cost and time while increasing reproducibility. More importantly, our approach enabled quantitative differentiation of homing choices of breast cancer cells.

Currently, the OoC platforms we present are limited by the choice of normal cell lines that can represent specific tissues. Although, the rat liver-derived cell line, BRL3A, attracted human breast cancer cells, we cannot exclude the possibility that human liver-derived cells might provide a more compatible environment for the invasion and extravasation of human cancer cells. MCF10A cells were selected to represent normal breast tissue due to their ability to form polarized acini in 3D basement membrane cultures (Debnath et al., 2003). It should be noted that MCF10A cells might develop a better environment for cancer cell attraction if supported by normal or cancer-associated fibroblasts. However, the current choice of cell lines provided the advantage of culturing with simple DMEM medium without addition of any specific growth factors to maintain the system. This allowed the IC- and EX-Chips to assess the effects of different homing cells independent of the medium components. Nevertheless, including different tissue components such as epithelial cells, fibroblasts, adipocytes, and immune cells should be further investigated to improve the microenvironment model.

Triple-negative breast cancer preferentially metastasizes to the lung and liver (Al-Mahmood et al., 2018; Chu et al., 2014). Consistent with published clinical data, invasion/chemotaxis results here showed that MDA-MB-231 cells, which are the triple-negative subtype, preferred lung and liver microenvironments over the breast



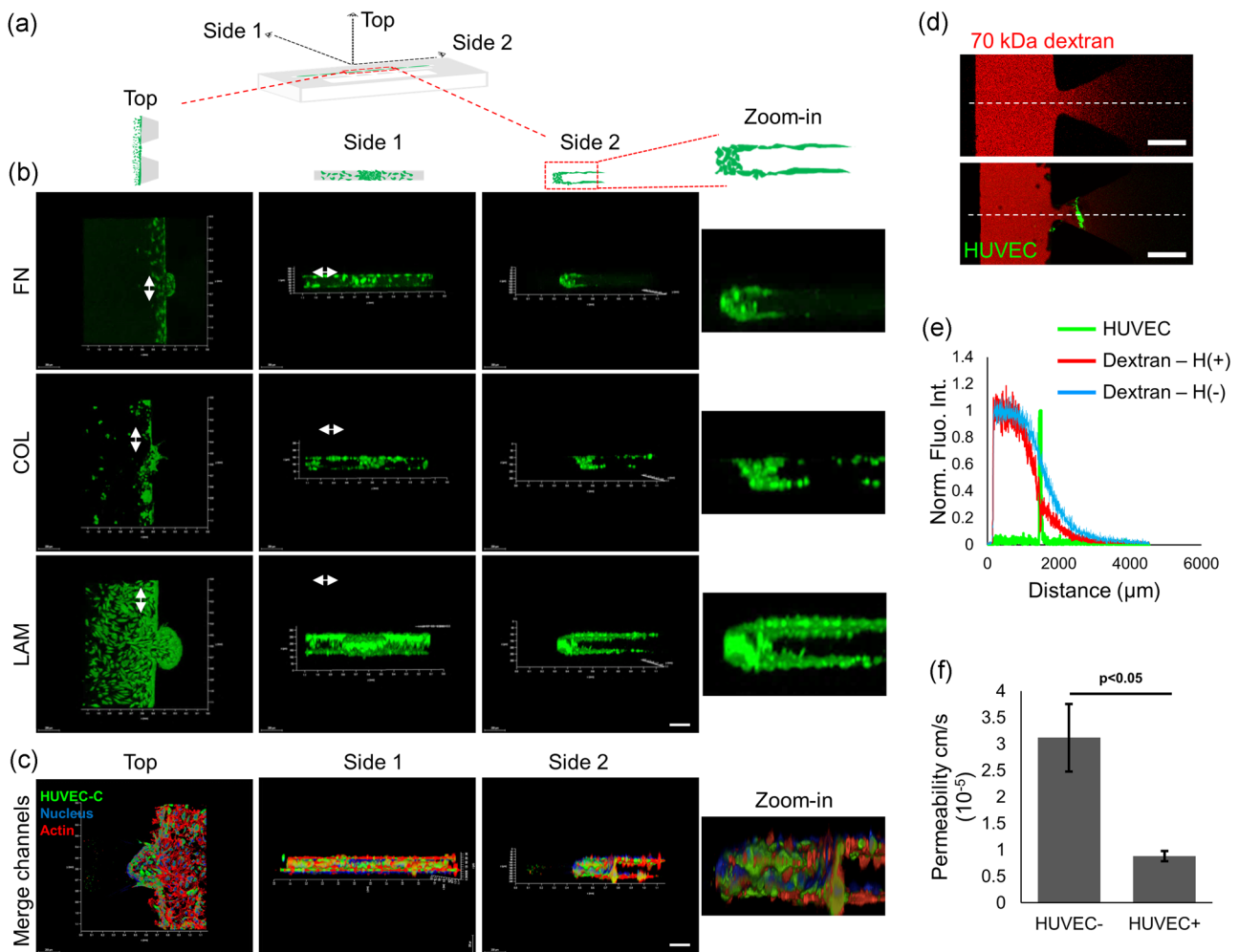


**FIGURE 4** Generation of an intact endothelial monolayer. (a) Schematic of 3D Ex-chip with different views defined as Top, Side1 and Side 2. (b) Representative 3D images showing endothelial cells (green) on fibronectin (FN), collagen type I (COL), and laminin (LAM)-coated surfaces. The post gaps are marked with two-sided arrows in different views; scale bar = 200  $\mu\text{m}$ . (c) Confocal images showing actin (phalloidin), nuclei (4',6-diamidino-2-phenylindole [DAPI]), human umbilical vein endothelial cell line (HUVEC-C) (cell tracker) in red, blue, and green, respectively, from different views in APTES-LAM-coated EX-chip; scale bar = 200  $\mu\text{m}$ . (d) Representative images of post-gap regions in 70 kDa fluorescent dextran (red) loaded chips in the absence (top panel) and the presence (bottom panel) of an endothelial monolayer (green); scale bar = 500  $\mu\text{m}$ . (e) Normalized fluorescent intensity profiles along the dashed lines. HUVEC-C signal (green), dextran signal in the absence (blue) and presence (red) of HUVEC-C. (f) Permeability for 70 kDa dextran in the absence and presence of HUVEC-C

microenvironment. What is more, the lung metastatic subclone MDA-MB-231 LM2, showed invasion/chemotaxis preferentially to the lung microenvironment, consistent with previous *in vivo* studies (Minn et al., 2005). Parental MDA-MB-231 cells also showed a similar trend suggesting that the lung-specific metastatic cells could be more populated in the parental MDA-MB-231 cell line. Taken together, these results highlight the ability of the IC-chip to quantitatively determine the invasion/chemotaxis potential of cancer cells towards different target sites and to distinguish between cancer cells with different *in vivo* metastatic behaviors.

The generation of an intact endothelial monolayer allows mimicking the blood vessel interface (Shenoy & Lu, 2016). However, the hydrophobic nature of cured PDMS require surface modifications such as APTES and PLL coatings (Leivo et al., 2017). To optimize the formation of

an intact endothelial monolayer, laminin, which is a component of the basement membrane, collagen type I, which is abundant in connective tissue and FN, a common extracellular matrix protein, were tested on the APTES pre-coated interior PDMS surfaces of EX-chips. Among the three different proteins, laminin promoted endothelial cell adhesion most. This is probably because endothelial cells *in vivo* exist on a basement membrane, of which laminin is a marked component.

The permeability values for *in vitro* networks of endothelial cells or *in vivo* conditions (Dreher et al., 2006; Shirure et al., 2018; Sobrino et al., 2016; Yuan et al., 2009) are one or two orders of magnitude lower than those calculated for the EX-chips in this study which are yet in agreement with previous studies using an endothelial monolayer for the extravasation interface (Frost et al., 2019; Jeon et al., 2013; van Duinen et al., 2017; Zervantonakis et al., 2012). The difference between the nature of

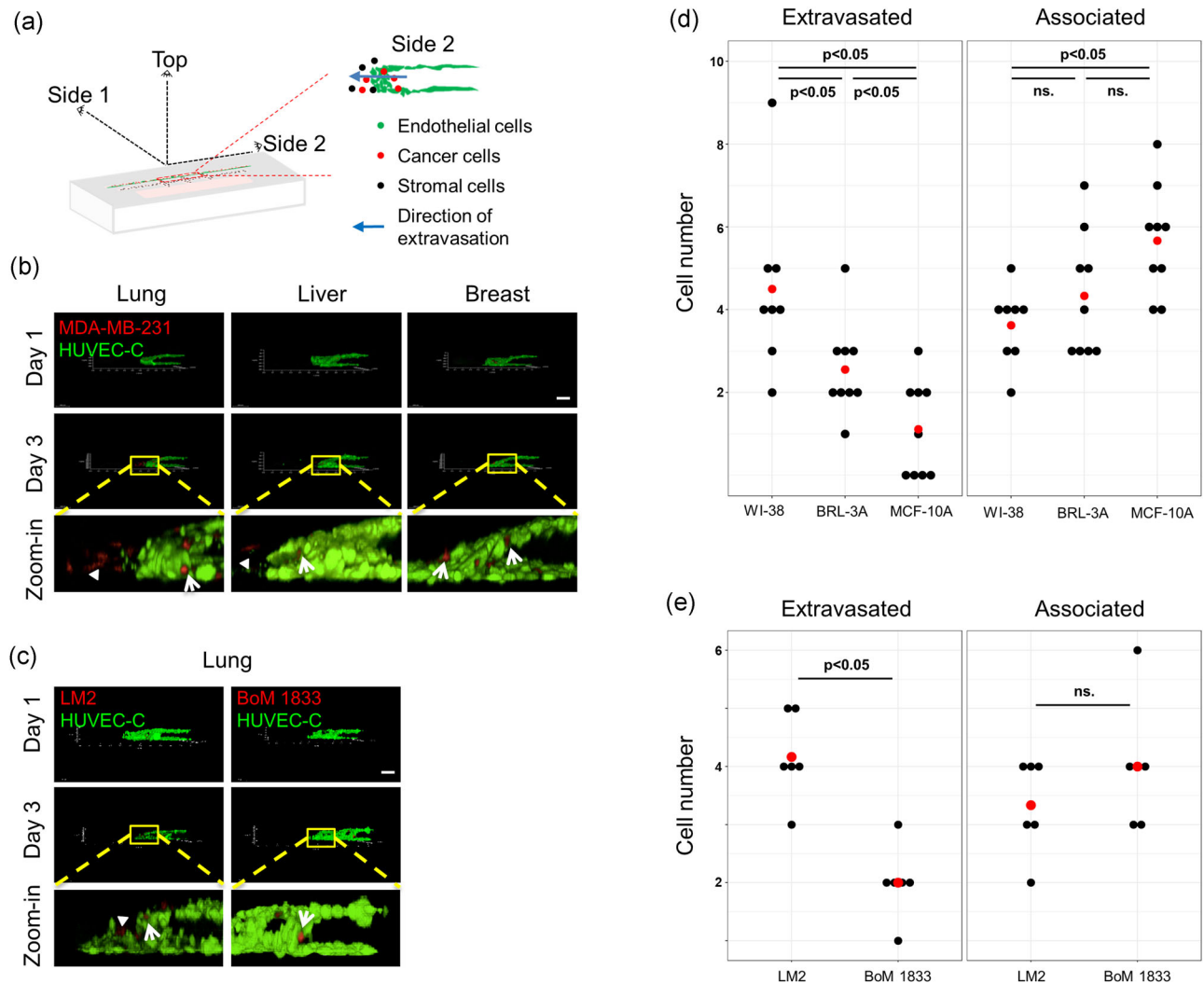


**FIGURE 5** Extravasation of metastatic breast cancer cells into the lung, liver and breast microenvironments. (a) Schematic of 3D Ex-chip with different views defined as Top, Side1, Side 2 and an annotated sample Side 2 view. (b) Representative Z-stack projection images showing Side 2 views of endothelial monolayers of HUVEC-C cells (green) and extravasated (arrow head) and associated (arrow) MDA-MB-231 cells (red) into the lung, liver or breast microenvironments; scale bar = 200  $\mu\text{m}$ . (c) Representative Z-stack projection images showing Side 2 views of endothelial monolayers of HUVEC-C cells (green) and extravasated (arrow head) and associated (arrow) MDA-MB-231 LM2 and BoM 1833 cells (red) into the lung microenvironment; scale bar = 200  $\mu\text{m}$ . The number of extravasated and associated (d) MDA-MB-231 cells to lung, liver, and breast microenvironments ( $n = 9$ ) and (e) MDA MB 231 LM2 and BoM 1833 to lung microenvironment ( $n = 6$ ). Each black dot represents the cell number for one post-gap within the EX-chip, while the red dot is the average number of cells for each condition

the endothelial cell organization, that is, a network versus a monolayer is probably the reason for the difference (Offeddu et al., 2019). Nonetheless, the permeability of the EX-chips would not allow cell passage. Furthermore, since EMC contains serum-free medium, an input from, for example, growth factors or chemokines is not present to affect permeability or molecular interactions that will facilitate passage of cancer cells. However, release of chemokines from HMC to EMC might induce extravasation, which in turn is an advantage of the EX-chip set-up in terms of mimicking the in vivo conditions.

Finally, both the invasion/chemotaxis and extravasation assays showed that MDA-MB-231 cells preferred the lung microenvironment significantly more than the other target

microenvironments. Although the MDA-MB-231 cells invaded towards the breast microenvironment on the IC-chip, they did not extravasate into the same microenvironment. These findings indicate that IC-chip would be useful to predict invasive behavior of the cancer cells in the primary tumor site as well as their preference for different target tissues. On the other hand, EX-chip would be more relevant and efficient for the determination of the overall metastatic potential and the homing choices of breast cancer cells.

In conclusion, we developed two OoC platforms based on the IC-chip and EX-chip, to comparatively and quantitatively determine the invasion/chemotaxis and extravasation phenotypes of different breast cancer cells to lung, liver, and breast microenvironments. Determination

of tissue-specific metastatic potential of breast cancer cells is expected to improve diagnosis and help select the ideal therapy.

## ACKNOWLEDGMENTS

This study was supported by the grant numbered 115E057 from Scientific and Technological Research Council of Turkey (TUBITAK). The authors thank Joan Massagué and Memorial Sloan Kettering Cancer Center for providing MDA-MB-231 LM2 and MDA-MB-231 1833-BoM cell lines.

## CONFLICT OF INTERESTS

Devrim Pesen-Okvur was the co-founder and Ozden Yalcin-Ozuysal was the scientific advisor of Initio Biomedical Engineering (Turkey).

## AUTHOR CONTRIBUTIONS

Burcu Firatligil-Yildirim and Gizem Bati-Ayaz: *methodology, formal analysis, investigation, writing-original draft, visualization*; Ismail Tahmaz and Muge Bilgen: *methodology, investigation, formal analysis, writing-original draft*; Devrim Pesen-Okvur and Ozden Yalcin-Ozuysal: *methodology, conceptualization, software, formal analysis, resources, writing-original draft, writing-review and editing, supervision, project administration, funding acquisition*.

## DATA AVAILABILITY STATEMENT

The raw data and processed data required to reproduce these findings are available from the corresponding author upon request.

## ORCID

Devrim Pesen-Okvur  <https://orcid.org/0000-0001-8333-4193>

Ozden Yalcin-Ozuysal  <http://orcid.org/0000-0003-0552-368X>

## REFERENCES

- Al-Mahmood, S., Sapiezynski, J., Garbuzenko, O. B., & Minko, T. (2018). Metastatic and triple-negative breast cancer: Challenges and treatment options. *Drug Delivery and Translational Research*, 8(5), 1483–1507. <https://doi.org/10.1007/s13346-018-0551-3>
- Bersini, S., Jeon, J. S., Dubini, G., Arrigoni, C., Chung, S., Charest, J. L., Moretti, M., & Kamm, R. D. (2014). A microfluidic 3D in vitro model for specificity of breast cancer metastasis to bone. *Biomaterials*, 35(8), 2454–2461. <https://doi.org/10.1016/j.biomaterials.2013.11.050>
- Bi, Y., Shirure, V. S., Liu, R., Cunningham, C., Ding, L., Meacham, J. M., Goedegebuure, S. P., George, S. C., & Fields, R. C. (2020). Tumor-on-a-chip platform to interrogate the role of macrophages in tumor progression. *Integrative Biology*, 12(9), 221–232. <https://doi.org/10.1093/intbio/zyaa017>
- Bos, P. D., Zhang, X. H., Nadal, C., Shu, W., Gomis, R. R., Nguyen, D. X., Minn, A. J., van de Vijver, M. J., Gerald, W. L., Foekens, J. A., & Massagué, J. (2009). Genes that mediate breast cancer metastasis to the brain. *Nature*, 459(7249), 1005–1009. <https://doi.org/10.1038/nature08021>
- Boussommier-Calleja, A., Atiyas, Y., Haase, K., Headley, M., Lewis, C., & Kamm, R. D. (2019). The effects of monocytes on tumor cell extravasation in a 3D vascularized microfluidic model. *Biomaterials*, 198, 180–193. <https://doi.org/10.1016/j.biomaterials.2018.03.005>
- Chen, M. B., Whisler, J. A., Fröse, J., Yu, C., Shin, Y., & Kamm, R. D. (2017). On-chip human microvasculature assay for visualization and quantification of tumor cell extravasation dynamics. *Nature Protocols*, 12(5), 865–880. <https://doi.org/10.1038/nprot.2017.018>
- Chen, M.-T., Sun, H.-F., Zhao, Y., Fu, W.-Y., Yang, L.-P., Gao, S.-P., Li, L.-D., Jiang, H.-L., & Jin, W. (2017). Comparison of patterns and prognosis among distant metastatic breast cancer patients by age groups: a SEER population-based analysis. *Scientific Reports*, 7, (1). <https://doi.org/10.1038/s41598-017-10166-8>
- Chu, J. E., Xia, Y., Chin-Yee, B., Goodale, D., Croker, A. K., & Allan, A. L. (2014). Lung-derived factors mediate breast cancer cell migration through CD44 receptor-ligand interactions in a novel ex vivo system for analysis of organ-specific soluble proteins. *Neoplasia*, 16(2), 180–191. <https://doi.org/10.1593/neo.132076>
- Debnath, J., Muthuswamy, S. K., & Brugge, J. S. (2003). Morphogenesis and oncogenesis of MCF-10A mammary epithelial acini grown in three-dimensional basement membrane cultures. *Methods*, 30(3), 256–268. [https://doi.org/10.1016/s1046-2023\(03\)00032-x](https://doi.org/10.1016/s1046-2023(03)00032-x)
- Dreher, M. R., Liu, W. G., Michelich, C. R., Dewhirst, M. W., Yuan, F., & Chilkoti, A. (2006). Tumor vascular permeability, accumulation, and penetration of macromolecular drug carriers. *Journal of the National Cancer Institute*, 98(5), 335–344. <https://doi.org/10.1093/jnci/djj070>
- Fares, J., Fares, M. Y., Khachfe, H. H., Salhab, H. A., & Fares, Y. (2020). Molecular principles of metastasis: A hallmark of cancer revisited. *Signal Transduction and Targeted Therapy*, 5(1), 28. <https://doi.org/10.1038/s41392-020-0134-x>
- Frost, T. S., Jiang, L., Lynch, R. M., & Zohar, Y. (2019). Permeability of epithelial/endothelial barriers in transwells and microfluidic bilayer devices. *Micromachines*, 10(8). <https://doi.org/10.3390/mi10080533>
- Guo, S., & Deng, C. X. (2018). Effect of stromal cells in tumor microenvironment on metastasis initiation. *International Journal of Biological Sciences*, 14(14), 2083–2093. <https://doi.org/10.7150/ijbs.25720>
- Howlander, N. N. A., Krapcho, M., Miller, D., Brest, A., Yu, M., Ruhl, J., Tatalovich, Z., Mariotto, A., Lewis, D. R., Chen, H. S., Feuer, E. J., & Cronin, K. A. (2020). Cancer of the female breast (invasive): 5-year relative and period survival by race, diagnosis year, age and stage at diagnosis. *SEER Cancer Statistics Review*. Retrieved from [https://seer.cancer.gov/csr/1975\\_2017/](https://seer.cancer.gov/csr/1975_2017/)
- Ilhan, M., Kucukkose, C., Efe, E., Gunyuz, Z. E., Firatligil, B., Dogan, H., Ozuysal, M., & Yalcin-Ozuysal, O. (2020). Pro-metastatic functions of Notch signaling is mediated by CYR61 in breast cells. *European Journal of Cell Biology*, 99(2-3), 151070. <https://doi.org/10.1016/j.ejcb.2020.151070>
- Jeon, J. S., Bersini, S., Gilardi, M., Dubini, G., Charest, J. L., Moretti, M., & Kamm, R. D. (2015). Human 3D vascularized organotypic microfluidic assays to study breast cancer cell extravasation. *Proceedings of the National Academy of Sciences*, 112(1), 214–219. <https://doi.org/10.1073/pnas.1417115112>
- Jeon, J. S., Zervantonakis, I. K., Chung, S., Kamm, R. D., & Charest, J. L. (2013). In vitro model of tumor cell extravasation. *PLOS One*, 8(2), e56910. <https://doi.org/10.1371/journal.pone.0056910>
- Jin, L., Han, B., Siegel, E., Cui, Y., Giuliano, A., & Cui, X. (2018). Breast cancer lung metastasis: Molecular biology and therapeutic implications. *Cancer Biology & Therapy*, 19(10), 858–868. <https://doi.org/10.1080/15384047.2018.1456599>
- Kang, Y., He, W., Tulley, S., Gupta, G. P., Serganova, I., Chen, C.-R., Manova-Todorova, K., Blasberg, R., Gerald, W. L., & Massagué, J. (2005). Breast cancer bone metastasis mediated by the Smad tumor suppressor pathway. *Proceedings of the National Academy of Sciences of the United States of America*, 102(39), 13909–13914. <https://doi.org/10.1073/pnas.0506517102>
- Kimura, H., Sakai, Y., & Fujii, T. (2018). Organ/body-on-a-chip based on microfluidic technology for drug discovery. *Drug Metabolism and Pharmacokinetics*, 33(1), 43–48. <https://doi.org/10.1016/j.dmpk.2017.11.003>

- Langley, R. R., & Fidler, I. J. (2011). The seed and soil hypothesis revisited--the role of tumor-stroma interactions in metastasis to different organs. *International Journal of Cancer*, 128(11), 2527–2535. <https://doi.org/10.1002/ijc.26031>
- Leivo, J., Virjula, S., Vanhatupa, S., Kartasalo, K., Kreutzer, J., Miettinen, S., & Kallio, P. (2017). A durable and biocompatible ascorbic acid-based covalent coating method of polydimethylsiloxane for dynamic cell culture. *Journal of the Royal Society, Interface*, 14(132). <https://doi.org/10.1098/rsif.2017.0318>
- Minn, A. J., Gupta, G. P., Siegel, P. M., Bos, P. D., Shu, W., Giri, D. D., Viale, A., Olshen, A. B., Gerald, W. L., & Massagué, J. (2005). Genes that mediate breast cancer metastasis to lung. *Nature*, 436(7050), 518–524. <https://doi.org/10.1038/nature03799>
- Myers, D. R., Sakurai, Y., Tran, R., Ahn, B., Hardy, E. T., Mannino, R., Kita, A., Tsai, M., & Lam, W. A. (2012). Endothelialized microfluidics for studying microvascular interactions in hematologic diseases. *Journal of Visualized Experiments*, 64, 3958. <https://doi.org/10.3791/3958>
- Offeddu, G. S., Haase, K., Gillrie, M. R., Li, R., Morozova, O., Hickman, D., Knutson, C. G., & Kamm, R. D. (2019). An on-chip model of protein paracellular and transcellular permeability in the microcirculation. *Biomaterials*, 212, 115–125. <https://doi.org/10.1016/j.biomaterials.2019.05.022>
- Ozdil, B., Onal, S., Oruç, T., & Pesen Okvur, D. (2014). Fabrication of 3D controlled in vitro microenvironments. *Methods*, 1, 60–66. <https://doi.org/10.1016/j.mex.2014.06.003>
- Paget, S. (1889). The distribution of secondary growths in cancer of the breast. *The Lancet*, 133(3421), 571–573. [https://doi.org/10.1016/S0140-6736\(00\)49915-0](https://doi.org/10.1016/S0140-6736(00)49915-0)
- Pathak, A., & Kumar, S. (2012). Independent regulation of tumor cell migration by matrix stiffness and confinement. *Proceedings of the National Academy of Sciences of the United States of America*, 109(26), 10334–10339. <https://doi.org/10.1073/pnas.1118073109>
- Peck, R. W., Hinojosa, C. D., & Hamilton, G. A. (2020). Organs-on-chips in clinical pharmacology: Putting the patient into the center of treatment selection and drug development. *Clinical Pharmacology & Therapeutics*, 107(1), 181–185. <https://doi.org/10.1002/cpt.1688>
- Polacheck, W. J., Charest, J. L., & Kamm, R. D. (2011). Interstitial flow influences direction of tumor cell migration through competing mechanisms. *Proceedings of the National Academy of Sciences of the United States of America*, 108(27), 11115–11120. <https://doi.org/10.1073/pnas.1103581108>
- Rodrigues, R. O., Sousa, P. C., Gaspar, J., Bañobre-López, M., Lima, R., & Minas, G. (2020). Organ-on-a-chip: A preclinical microfluidic platform for the progress of nanomedicine. *Small*, 16(51), 2003517. <https://doi.org/10.1002/sml.202003517>
- Roussos, E. T., Condeelis, J. S., & Patsialou, A. (2011). Chemotaxis in cancer. *Nature Reviews Cancer*, 11(8), 573–587. <https://doi.org/10.1038/nrc3078>
- Shenoy, A. K., & Lu, J. (2016). Cancer cells remodel themselves and vasculature to overcome the endothelial barrier. *Cancer Letters*, 380(2), 534–544. <https://doi.org/10.1016/j.canlet.2014.10.031>
- Shirure, V. S., Bi, Y., Curtis, M. B., Lezia, A., Goedegebuure, M. M., Goedegebuure, S. P., Aft, R., Fields, R. C., & George, S. C. (2018). Tumor-on-a-chip platform to investigate progression and drug sensitivity in cell lines and patient-derived organoids. *Lab on a Chip*, 18(23), 3687–3702. <https://doi.org/10.1039/c8lc00596f>
- Sobrinho, A., Phan, D. T., Datta, R., Wang, X., Hachey, S. J., Romero-López, M., Gratton, E., Lee, A. P., George, S. C., & Hughes, C. C. (2016). 3D microtumors in vitro supported by perfused vascular networks. *Scientific Reports*, 6, 6. <https://doi.org/10.1038/srep31589>
- Song, J. W., Cavnar, S. P., Walker, A. C., Luker, K. E., Gupta, M., Tung, Y.-C., Luker, G. D., & Takayama, S. (2009). Microfluidic endothelium for studying the intravascular adhesion of metastatic breast cancer cells. *PLOS One*, 4(6), e5756. <https://doi.org/10.1371/journal.pone.0005756>
- Soscia, D., Belle, A., Fischer, N., Enright, H., Sales, A., Osburn, J., Benett, W., Mukerjee, E., Kulp, K., Pannu, S., & Wheeler, E. (2017). Controlled placement of multiple CNS cell populations to create complex neuronal cultures. *PLOS One*, 12(11), e0188146. <https://doi.org/10.1371/journal.pone.0188146>
- Truong, D., Puleo, J., Llave, A., Mouneimne, G., Kamm, R. D., & Nikkhah, M. (2016). Breast cancer cell invasion into a three dimensional tumor-stroma microenvironment. *Scientific Reports*, 6(1), 34094. <https://doi.org/10.1038/srep34094>
- van Den Berg, A., Mummery, C. L., Passier, R., & van der Meer, A. D. (2019). Personalised organs-on-chips: Functional testing for precision medicine. *Lab on a Chip*, 19(2), 198–205. <https://doi.org/10.1039/c8lc00827b>
- van Duinen, V., van den Heuvel, A., Trietsch, S. J., Lanz, H. L., van Gils, J. M., van Zonneveld, A. J., Vulto, P., & Hankemeier, T. (2017). 96 perfusable blood vessels to study vascular permeability in vitro. *Scientific Reports*, 7(1), 18071. <https://doi.org/10.1038/s41598-017-14716-y>
- Vickerman, V., & Kamm, R. D. (2012). Mechanism of a flow-gated angiogenesis switch: early signaling events at cell-matrix and cell-cell junctions. *Integrative Biology*, 4(8), 863–874. <https://doi.org/10.1039/c2ib00184e>
- Wang, R., Zhu, Y., Liu, X., Liao, X., He, J., & Niu, L. (2019). The clinicopathological features and survival outcomes of patients with different metastatic sites in stage IV breast cancer. *BMC Cancer*, 19(1), 1091. <https://doi.org/10.1186/s12885-019-6311-z>
- Wu, Q., Liu, J., Wang, X., Feng, L., Wu, J., Zhu, X., Wen, W., & Gong, X. (2020). Organ-on-a-chip: Recent breakthroughs and future prospects. *Biomedical Engineering Online*, 19(1), 9. <https://doi.org/10.1186/s12938-020-0752-0>
- Yalcin-Ozuyal, O., Fiche, M., Guitierrez, M., Wagner, K. U., Raffoul, W., & Briskin, C. (2010). Antagonistic roles of Notch and p63 in controlling mammary epithelial cell fates. *Cell Death and Differentiation*, 17(10), 1600–1612. <https://doi.org/10.1038/cdd.2010.37>
- Yuan, W., Lv, Y. G., Zeng, M., & Fu, B. M. (2009). Non-invasive measurement of solute permeability in cerebral microvessels of the rat. *Microvascular Research*, 77(2), 166–173. <https://doi.org/10.1016/j.mvr.2008.08.004>
- Zengin, T., Ekinci, B., Kucukkose, C., & Yalcin-Ozuyal, O. J. P. O. (2015). IRF6 is involved in the regulation of cell proliferation and transformation in MCF10A cells downstream of notch signaling. *PLOS One*, 10, e0132757. <https://doi.org/10.1371/journal.pone.0132757>
- Zervantonakis, I. K., Hughes-Alford, S. K., Charest, J. L., Condeelis, J. S., Gertler, F. B., & Kamm, R. D. (2012). Three-dimensional microfluidic model for tumor cell intravasation and endothelial barrier function. *Proceedings of the National Academy of Sciences of the United States of America*, 109(34), 13515–13520. <https://doi.org/10.1073/pnas.1210182109>

## SUPPORTING INFORMATION

Additional Supporting Information may be found online in the supporting information tab for this article.

**How to cite this article:** Firatligil-Yildirim, B., Bati-Ayaz, G., Tahmaz, I., Bilgen, M., Pesen-Okvur, D., & Yalcin-Ozuyal, O. (2021). On-chip determination of tissue-specific metastatic potential of breast cancer cells. *Biotechnology and Bioengineering*, 118, 3799–3810. <https://doi.org/10.1002/bit.27855>